PNAS RESEARCH ARTICLE | PHYSICS

Spin–orbit exciton–induced phonon chirality in a quantum magnet

David Lujan[a,b,1], Jeongheon Choe[a,b,1], Swati Chaudhary[a,c,d,1], Gaihua Ye[e], Cynthia Nnokwe[e], Martin Rodriguez-Vega[a,c], Jiaming He[f], Frank Y. Gao[a,b], T. Nathan Nunley[a,b], Edoardo Baldini[a,b], Jianshi Zhou[b,f], Gregory A. Fiete[c,d], Rui He[e,2], and Xiaoqin Li[a,b,2]

Edited by Hui Deng, University of Michigan, Ann Arbor, MI; received March 16, 2023; accepted November 17, 2023, by Editorial Board Member Hui Cao

The interplay of charge, spin, lattice, and orbital degrees of freedom in correlated materials often leads to rich and exotic properties. Recent studies have brought new perspectives to bosonic collective excitations in correlated materials. For example, inelastic neutron scattering experiments revealed non-trivial band topology for magnons and spin–orbit excitons (SOEs) in a quantum magnet $CoTiO_3$ (CTO). Here, we report phonon properties resulting from a combination of strong spin–orbit coupling, large crystal field splitting, and trigonal distortion in CTO. Specifically, the interaction between SOEs and phonons endows chirality to two E_g phonon modes and leads to large phonon magnetic moments observed in magneto-Raman spectra. The remarkably strong magneto-phononic effect originates from the hybridization of SOEs and phonons due to their close energy proximity. While chiral phonons have been associated with electronic topology in some materials, our work suggests opportunities may arise by exploring chiral phonons coupled to topological bosons.

chirality | topology | correlated materials | Raman spectroscopy | phonons

Significance

Phonons are known as an important energy carrier and their interaction with electrons is critical for understanding exotic properties in correlated materials. They typically do not carry angular momentum or respond to an external magnetic field. Chiral phonons arising from circular ionic motions alone would only exhibit a small magnetic moment. In contrast, chiral phonons reported recently in several classes of materials including the pseudogap phase of cuprates and topological semimetals exhibit surprisingly large moments. Here, we report studies of chiral phonons in $CoTiO_3$, a quantum magnet that hosts interesting bosonic excitations such as topological magnons and spin–orbit excitons (SOEs). The observed phonon chirality is attributed to phonon and SOE hybridization.

Chiral phonons refer to circular ionic motions that lead to a non-zero phonon angular momentum. Following this simple picture, chiral phonons should only respond to an applied magnetic field very weakly and feature a phonon magnetic moment on the order of a few nuclear magnetons. This simple estimate is, however, three orders of magnitude smaller than that observed in several classes of materials (1–6). Thus, to correctly describe the phonon magnetic moment, the coupling between phonons and electronic degrees of freedom must be taken into account. Electrons can endow chiral phonons with a magnetic moment through two possible mechanisms: i) phonon-induced adiabatic evolution of electronic states (7, 8) and ii) phonon-induced mixing of different electronic energy levels (9–12).

When electronic and lattice vibration energies are very different, the first mechanism is in effect. Phonon modes induce adiabatic evolution of electronic states, typically described within the Born–Oppenheimer approximation. This phonon-mediated electronic magnetization has both spin and orbital components. For the orbital component, both topologically trivial and non-trivial electronic states should contribute to the phonon magnetic moment (7). A significant electronic topology contribution to chiral phonons has only been identified very recently in topological semimetals (e.g., Cd_3As_2) (13) and insulating thin films (e.g., $Pb_{1-x}Sn_xTe$) (6). On the other hand, when the electronic excitations are in close proximity to the phonon energy, the second mechanism of electronic hybridization applies. In magnetic materials, low-energy electronic excitations energetically close to phonons can originate from crystal-electric field (CEF) and spin–orbit effects from the magnetic ions. Such spin and orbital degrees of freedom respond strongly to magnetic fields, and their hybridization with phonons can result in a substantial phonon magnetic moment (1, 14–18).

Here, we report the observation of large magnetic moments associated with two E_g phonons in the 3D quantum magnet CTO via helicity-resolved spontaneous Raman scattering. The superposition of two degenerate linearly polarized components of an E_g mode with a $\pi/2$ phase difference leads to a chiral mode. The degeneracy of an E_g mode is lifted by a magnetic field applied in a direction perpendicular to the plane of circular ionic motions. From the field-dependent energy splitting ($\Delta E_g = 2g_{ph}\mu_B B$) of two E_g modes, we extract their g_{ph} factors to be 1.11 ± 0.01 and 0.29 ± 0.01, respectively, at 12 K. We attribute the origin of the phonon chirality to hybridization with spin–orbit excitons (SOEs) mediated by orbital-lattice interactions. Our model explains the different g_{ph} factors of two chiral phonon modes and the persistence of phonon Zeeman splitting above the magnetic transition temperature.

Author contributions: E.B., R.H., and X.L. supervised D.L., J.C., G.Y., C.N., and F.Y.G. on the Raman experiments; X.L. and R.H. supervised D.L., J.C. and T.N.N. on Raman data analysis; J.Z. supervised J.H. on the crystal growth of the quantum magnet CoTiO3; M.R.-V. and G.A.F. supervised S.C. on the development of the toy model; and D.L., S.C., E.B., G.A.F., R.H., and X.L. wrote the paper.

The authors declare no competing interest.

This article is a PNAS Direct Submission. H.D. is a guest editor invited by the Editorial Board.

[1]D.L., J.C., and S.C. contributed equally to this work.

[2]To whom correspondence may be addressed. Email: rui.he@ttu.edu or elaineli@physics.utexas.edu.

This article contains supporting information online at https://www.pnas.org/lookup/suppl/doi:10.1073/pnas.2304360121/-/DCSupplemental.

Published March 8, 2024.

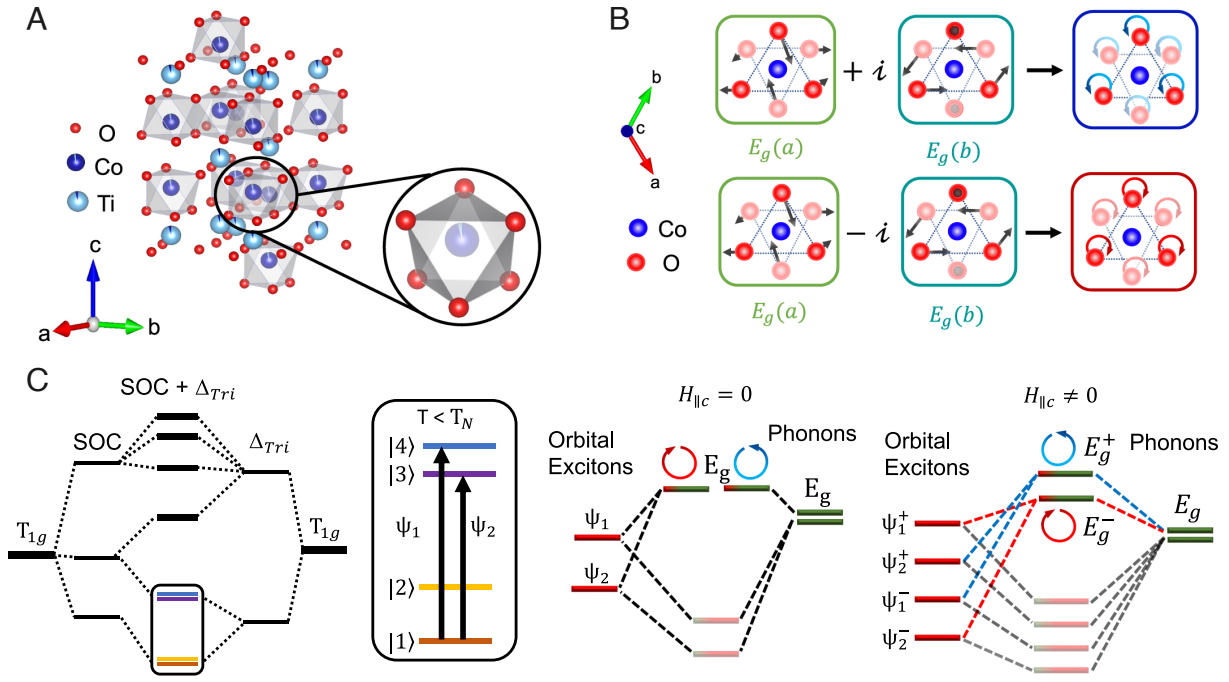

Fig. 1. Structures, electronic states, and phonon modes of $CoTiO_3$ (CTO). (*A*) Rhombohedral crystal structure of CTO with an inset of trigonally distorted oxygen atoms surrounding the cobalt atom. (*B*) Superposition of two linear vibrational modes in CTO resulting in two different chiral phonons. (*C*) (*Left*) Schematic energy-level diagram of the single-ion model taking into account spin–orbit coupling (SOC) and crystal field splitting (Δ_{Tri}). Details of the ground-state and first excited-state Kramers doublets are shown in the enclosed box. Below the Néel temperature, an exchange mean field splits lift the degeneracy of the Kramers doublets. Transitions between the ground- and first excited states give rise to multiple SOEs. (*Middle*) In the absence of an external magnetic field, the coupling between E_g phonons and SOEs (ψ_1 & ψ_2) induces phonon chirality but the phonon modes remain degenerate. (*Right*) An external magnetic field further lifts the degeneracy of the E_g phonons and separates the energies of four SOEs (ψ_1^+, ψ_2^+, ψ_1^-, ψ_2^-).

These findings also create venues for exploring the interplay of chiral phonons and topological bosons in correlated materials.

We first describe the lattice and spin structures of CTO and the phonon eigenvectors of interest. The Co^{2+} ions are arranged in slightly buckled two-dimensional honeycomb lattices. Along the *c*-axis, these honeycomb lattices are stacked in an ABC sequence with neighboring planes displaced diagonally by one third of the unit cell. Below the Néel temperature, T_N = 38 K, the magnetic moments order ferromagnetically within the *ab* planes and are coupled antiferromagnetically along the *c*-axis (19–21). CTO crystallizes in an ilmenite structure with a trigonal space group $R\bar{3}$. The Co^{2+} ions are surrounded by a trigonal distorted octahedral O^{2-} ions, as shown in Fig. 1*A*, leading to a crystal field splitting of ∼45 meV (20). Because the rhombohedral unit cell contains 10 ions, group theory predicts 10 Raman-active phonons at the Γ point of the Brillouin zone with 5 A_g modes and 5 E_g modes (22). The superposition of the two components of an E_g mode with a $\pi/2$ phase shift leads to a chiral mode that carriers angular momentum along the *c*-axis as illustrated in Fig. 1*B*.

Recent neutron scattering experiments on CTO have revealed SOEs (19–21) that are energetically close to some E_g phonon modes. Our study indicates that SOEs can hybridize with E_g phonon modes to impart chirality and a large magnetic moment. To describe this SOE-phonon coupling, we propose a model that focuses only on the two low-lying Kramers-doublets that are doubly degenerate in the absence of a magnetic field, as shown in the *Left* panel of Fig. 1*C*. The ground state manifold is predominantly composed of $|1,2\rangle = |J = 1/2, m_j = \pm 1/2\rangle$ and the excited states can be represented by $|3,4\rangle = |J = 3/2, m_j = \pm 3/2\rangle$. A SOE corresponds to a hole in the ground state manifold bound to an electron in the excited state manifolds. Below the Néel temperature, the exchange mean field lifts the Kramers ground and first excited state degeneracy such that two SOEs (ψ_1 and ψ_2) with energies of 25 meV (201 cm^{-1}) and 24.3 meV (196 cm^{-1}) can be observed. SOEs ψ_1 and ψ_2 correspond to transitions from the $|1\rangle$ ground state to the $|4\rangle$ and $|3\rangle$ excited states, respectively. In the absence of a magnetic field, the SOE-phonon hybridization leads to chiral E_g phonon modes as depicted in the *Middle* panel of Fig. 1*C*. The SOEs couple to E_g phonons but the phonon degeneracy is not lifted. When an external magnetic field is applied, both the degeneracy of the Kramers excited states and E_g phonons are lifted as illustrated in the *Right* panel of Fig. 1*C*, leading to four SOE states. The superscript + (−) describes the blue (red) shift from the original transition.

Results

We performed temperature-dependent Raman measurements to identify the relevant phonons and SOEs. Fig. 2 shows representative Raman spectra taken with the circular polarization combination of σ_- and σ_+ for incident and scattered photons. Raman active phonons, including 4 A_g and 5 E_g modes, predicted from group theory are identified in the spectra. The $A_g^{(4)}$ mode is too weak to be observed in the crossed-circular channel but detected in the co-circular channel (included in *SI Appendix*, Fig. S4). Because of the coupling between different degrees of freedom (i.e., electrons and phonons), the Raman selection rules of phonons in CTO do not follow simple rules determined by the crystal symmetry alone. Below T_N, two SOE modes ψ_1 at 201 cm^{-1} (25 meV) and ψ_2 at 195 cm^{-1} (24 meV) are observed. The splitting between these excitations results from the in-plane exchange mean-field that lifts the degeneracy of

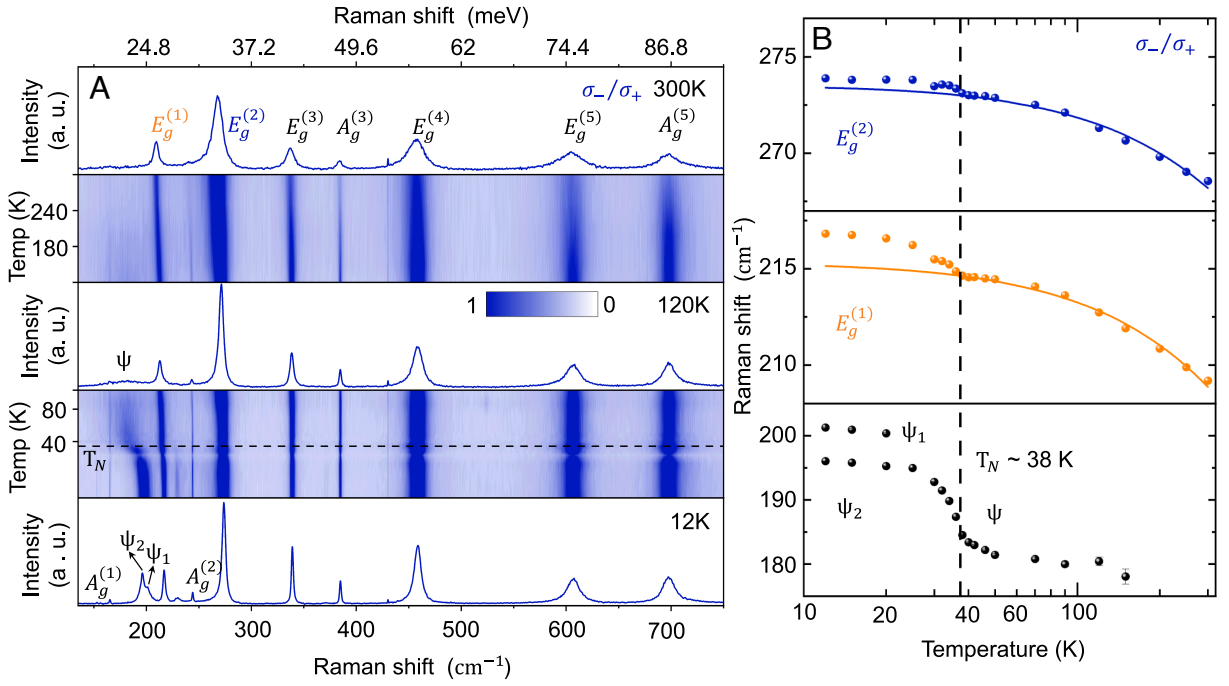

Fig. 2. Temperature dependent Raman spectra. (*A*) Raman spectra from 12 to 300 K in the σ_-/σ_+ polarization channel taken from a CTO sample with surface normal along the crystalline c-axis. Raman spectra at 12 K,120 K, and 300 K highlight the evolution of both phonons and SOEs. (*B*) The central frequency of E_g^1, E_g^2, and SOEs (ψ_1, ψ_2, ψ) as a function of temperature in the σ_-/σ_+ polarization channel. The solid lines for $E_g^{(1)}$ and $E_g^{(2)}$ correspond to fitting to the anharmonic model applicable to $T > T_N$. Error bars are smaller than the displayed data points.

the Kramers ground and first excited state. In recent neutron scattering experiments, only the splitting of the Kramers ground state has been observed partially due to limited energy resolution (20, 21). Above T_N, SOEs persist and broaden in spectral width. Since the exchange mean-field is modified in the absence of antiferromagnetic order, we use a different notation to represent the SOEs. Both $E_g^{(1)}$(orange) and $E_g^{(2)}$(blue) modes are energetically close to these SOEs and this proximity allows for hybridization between these collective modes. Our model predicts a strong Zeeman energy shift for both E_g phonons, and we expect $E_g^{(1)}$ to exhibit a larger magnetic moment than $E_g^{(2)}$ based on their resonant energy difference.

To quantitatively evaluate spin-lattice coupling, we analyze the temperature-dependent phonon frequencies in the absence of a magnetic field (Fig. 2*B*). The deviation from the anharmonic model for both $E_g^{(1)}$ and $E_g^{(2)}$ mode is about 1.66 cm^{-1} and 0.46 cm^{-1}, respectively, and it serves to justify the spin-lattice coupling. In contrast, an adjacent A_g mode at 244 cm^{-1} exhibits no such frequency deviation from the anharmonic model (data shown in *SI Appendix*, Fig. S3). Furthermore, the spin-lattice coupling in E_g modes is stronger as they become energetically closer to the SOEs, as shown in Fig. 2*A*. Above T_N, only one SOE mode ψ is observable up to ~150 K (19). The higher spin-lattice coupling of $E_g^{(1)}$ than that of $E_g^{(2)}$ results from its closer energy to the SOE modes. This interplay of energy scales is also reflected in the phonon magnetic moments as we present below. Chiral phonon modes correspond to the superposition of two components of an E_g mode vibrating in a plane perpendicular to the *c*-axis. Hence, a chiral E_g phonon can carry angular momentum along the *c*-axis but not along the *a*- or *b*-axis. Our model predicts that the E_g modes will only have a linear magnetic response to an external magnetic field applied along the *c*-axis. The Raman spectra taken with an external magnetic field applied along different crystal axes shown in Fig. 3 confirm this prediction. Fig. 3*A* shows helicity-resolved Raman spectra at a magnetic field of 7 T along the *c*-axis. The phonon energy blue shifts in the σ_-/σ_+ channel and red shifts in the opposite σ_+/σ_- channel, as illustrated in the energy diagram (Fig. 3*B*). In contrast, when the field is applied along either the *a*- or *b*-axis, the $E_g^{(2)}$ degeneracy is not lifted (Fig. 3 *C* and *D*), validating our model. Furthermore, in Raman spectra measured with an external field along the *c*-axis but with linearly polarized incident and scattered light, the $E_g^{(2)}$ modes do not split (*SI Appendix*, Fig. S5). In this case, the superposition between the two chiral phonon modes cancels the energy shift from each mode as the model predicts.

We analyze the angular momentum exchange in the σ_-/σ_+ Stokes process associated with an $E_g^{(2)}$ mode as illustrated in Fig. 3*B*. The modes that appear in the cross-circular channel change the photon angular momentum by $2\hbar$. A phonon carrying angular momentum $\hbar$ is created in the Stokes process. However, the three-fold rotational symmetry of the O^{-2} ions surrounding the Co^{2+} ions remedies the conservation of angular momentum (modulo $3\hbar$): $J_{pt}/\hbar + J_{ph}/\hbar = 0$ (Mod 3) (23–26). The phonons created in σ_-/σ_+ and σ_+/σ_- channel carry angular momentum, $J_{\mathrm{ph}} = \hbar$ and $J_{\mathrm{ph}} = -\hbar$, respectively (27). When an out-of-plane magnetic field is applied, the peaks corresponding to opposite angular momenta shift to different energies, which can be interpreted as the Zeeman splitting of the E_g modes. In the case of an in-plane field, there is no energy difference between the two cross-circular channels, which indicates the absence of a Zeeman effect for an in-plane μ_0H field as shown in Fig. 3*C*.

Finally, we investigate the Zeeman splitting of the $E_g^{(1)}$ and $E_g^{(2)}$ modes in the presence of an external magnetic field along

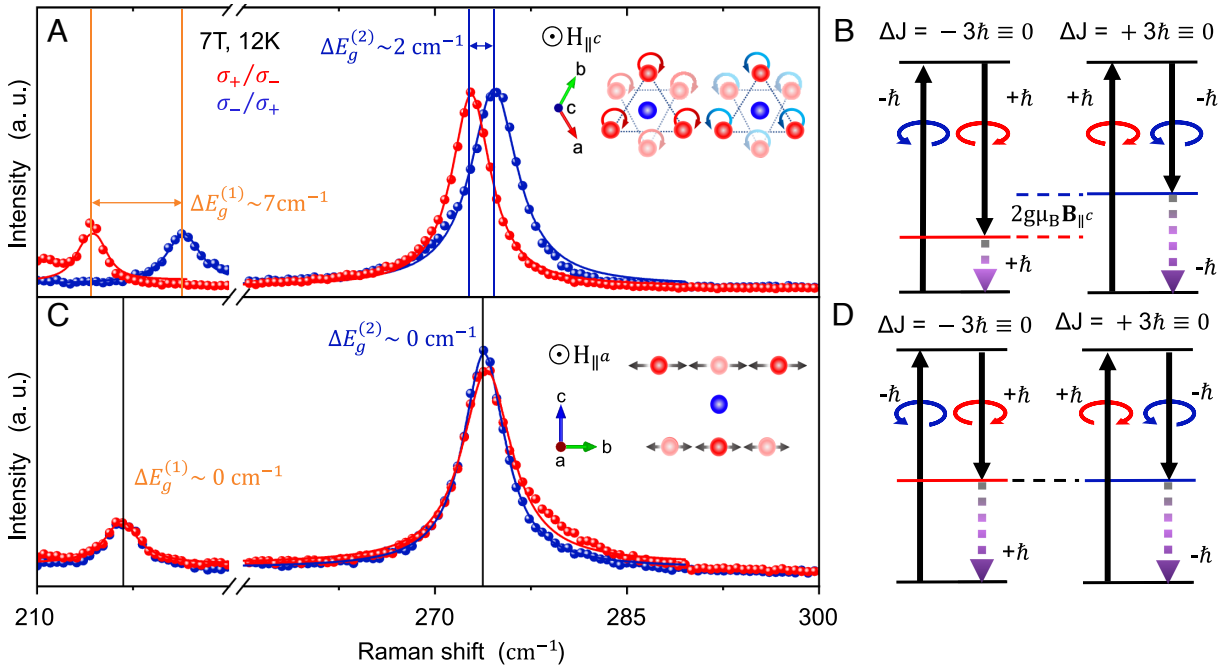

Fig. 3. Raman spectra taken with a magnetic field applied along different crystalline axes. (*A* and *C*) Circularly polarized Raman spectra taken at 12 K with a 7 T magnetic field applied to the surface normal along different crystalline axes [*c*-axis for panel (*A*) and *a*-axis for panel (*C*)]. The degeneracy of the E_g modes measured in σ_+/σ_- and σ_-/σ_+ channels is lifted (preserved) when a magnetic field is applied along *c*-axis (*a*-axes). *Insets*: Illustration of the O^{2-} ions' motion w.r.t. the applied magnetic field. (*B* and *D*) Angular momentum of incident, scattered photons and the phonon created in the Stokes process. The total angular momentum change is calculated by adding photon angular momentum change and that of the created phonon. A change of $\pm 3\ \hbar$ is equivalent to 0 due to the three-fold rotational symmetry of the magnetic lattice. In (*B*) the *Left* (σ_+/σ_-) and *Right* (σ_-/σ_+) diagrams represent the different $E_g^{(2)}$ phonon energies in the presence of a magnetic field along the *c*-axis. In (*D*), the angular momentum change in the Stokes process is the same as in (*B*), but the $E_g^{(2)}$ modes remain doubly degenerate in the presence of a magnetic field along the *a*-axis.

the *c*-axis at different temperatures. The spectra in Fig. 4*A* are taken at a magnetic field of 7 T and 12 K, where the Zeeman splitting is $\Delta E_g^{(1)} = 7.14 \pm 0.04$ cm^{-1} and $\Delta E_g^{(2)} = 2.03 \pm 0.03$ cm^{-1} for $E_g^{(1)}$ and $E_g^{(2)}$ mode, respectively. Magnetic order and non-trivial magnon topology can also give rise to phonon chirality and phonon-Zeeman splitting (28, 29). If the degeneracy of the $E_g^{(2)}$ mode in CTO is mainly lifted by the antiferromagnetic order, we would expect the phonon splitting to persist in the absence of magnetic field for $T < T_N$. The absence of phonon splitting below T_N in zero magnetic field and a significant Zeeman splitting ($\Delta E_g^{(1)} = 4.68 \pm 0.07$ cm^{-1} and $\Delta E_g^{(2)} = 1.59 \pm 0.01$ cm^{-1}) observed at 7 T and 50 K (Fig. 4*B*) suggest the dominant electronic contribution to the magnetic moments of both $E_g^{(1)}$ and $E_g^{(2)}$ modes. The Zeeman splitting of both E_g modes is no longer observable at room temperature where both electronic states in lower Kramers doublet are almost equally populated, and the effect of the magnetic field weakens significantly. This observation further justifies our conclusion that the phonon chirality is of electronic origin.

The splitting of both E_g modes as a function of the magnetic field along the *c*-axis (H_c) follows a simple linear relation, $\omega_{ph}^{\pm} = \Omega_+ \pm g_{ph}\mu_B H_c$. By fitting the slope, we extract $g_{ph} = 1.11 \pm 0.01$ (at 12 K), $g_{ph} = 0.68 \pm 0.01$ (at 50 K), and $g_{ph} \approx 0$ (at 300 K), respectively, for $E_g^{(1)}$. A systematic study of the temperature dependent g_{ph} for both $E_g^{(1)}$ and $E_g^{(2)}$ modes is summarized in Fig. 4*E*. For both E_g modes, as the temperature is lowered from 300 K, g_{ph} shows a sharp rise around T_N and then saturates at low temperature. This qualitative behavior is captured by our model calculation. We take into account two temperature-dependent factors in the model: population-difference of electronic states and the effective in-plane exchange magnetic field arising from the magnetic order below T_N. For $T > T_N$, as T increases, the population difference between two states in the lower Kramers doublet decreases, and thus the magnetic moment of phonons also decreases. For $T < T_N$, an additional effect from the temperature-dependent in-plane exchange magnetic field leads to the saturation of the phonon magnetic moment (*SI Appendix*). In our model, the E_g splitting is predicted to be directly proportional to spin imbalance resulting from the populated SOEs. While the theory agrees with the observed temperature dependent g_{ph} factor of $E_g^{(2)}$, it fails to reproduce the g_{ph} factor of the $E_g^{(1)}$ quantitatively. Our model omits several features including temperature-dependent lattice distortions and SOE energies, SOE band topology, and more importantly, SOEs' energies arising from spin-phonon coupling. The hybridization effect is stronger for a phonon mode closer in energy to SOEs. We quantify the degree of hybridization between phonons and SOEs in *SI Appendix*. Since $E_g^{(2)}$ is further off-resonance with SOEs, these factors contribute less sensitively to its g_{ph} factor.

Discussion

We summarize the observations of chiral phonons in previous studies. As discussed earlier, two common mechanisms responsible for chiral phonons are i) phonon-induced adiabatic

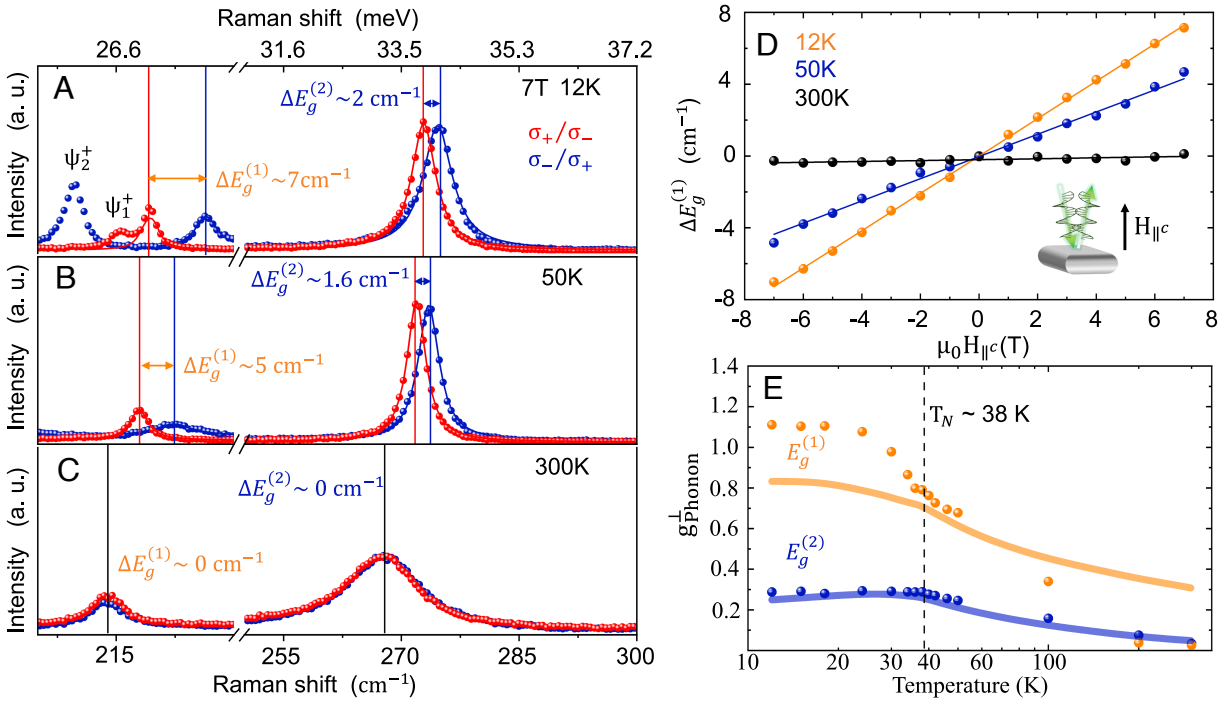

Fig. 4. Magnetic field-dependent Raman spectra and phonon g_{ph}-factor. (*A–C*) Raman spectra at 12, 50, and 300 K with an applied 7 T field along the *c*-axis. The red and blue solid lines are the Lorentzian function fittings for σ_+/σ_- (red) and σ_-/σ_+ (blue) circularly polarized channels, respectively. The vertical solid lines label the central peak positions. $\Delta E_g^{(1)}$ ($\Delta E_g^{(2)}$) represents the energy shift for opposite cross-circularly polarized Raman channels for $E_g^{(1)}$ ($E_g^{(2)}$) mode. (*D*) Summary of the energy shift difference $\Delta E_g^{(1)}$ as a function of magnetic field at three different temperatures. Solid lines are linear fits. (*E*) Temperature dependence of the phonon g_{ph}-factors. The solid lines are numeric calculations from our theoretical model. For (*D*) and (*E*), error bars displayed are smaller than the data points.

evolution of electronic states and ii) phonon-induced mixing of different electronic energy levels. In the former, phonon-mediated electronic magnetization has both spin and orbital components. The orbital component can be further separated into a non-topological and a topological part. A notable example of recent interest is that of transition metal dichalcogenide monolayers. In these inversion-symmetry broken honeycomb lattices, chiral phonons form at the zone-boundary at the K/K' valley, and they are topologically trivial (30, 31). Another example is $Pb_{1-x}Sn_{1-x}Te$ thin films, where a large phonon magnetic moment (1 to 3 Bohr magneton) emerges when the electronic bands become topologically non-trivial at $x > 0.32$ (6). In the Dirac semimetal Cd_3As_2, a large phonon magnetic moment develops via coupling to a cyclotron resonance over a range of applied magnetic fields when it shifts into resonance with the phonon mode (4). In the case of Cd_3As_2, the second mechanism of electronic hybridization gives rise to the observed phonon chirality.

To find examples more closely related to CTO, we survey other magnetic materials where the strong magnetic response of phonons may derive from coupling with different electronic excitations (1, 6, 7). In rare-earth materials where magnetism originates from *f* electrons, the CEF causes energy splittings between 4*f* levels that are close to phonon energies, imparting a large magnetic moment to phonons (2, 15). In materials where magnetism derives from *d* orbitals, CEF splitting is usually of the order of 1 eV, far exceeding the phonon energy. Spin–orbit splitting typically occurs at a lower energy than CEF splitting. In 5*d* systems like the iridates, SOC splitting is still at a much higher energy than phonons. In contrast, spin–orbit splitting in 3*d* systems is typically much smaller than optical phonon energies. Thus, CTO presents an example of 3*d* magnets where the combination of SOC and trigonal distortion leads to strong hybridization between phonons and SOEs.

The underlying mechanism for chiral phonons in CTO bears a strong resemblance to that of the phonon Zeeman effect observed in rare-earth trihalides where the phonon chirality and magnetic moment arise due to the hybridization of phonons with CEF split states (1, 2). In the case of CTO, the involvement of electronic states in this process is primarily influenced by SOC and trigonal distortion. The electronic excitations are comparable in energy to phonons and exchange interactions like "f" electron states in rare-earth systems (19). Moreover, CTO exhibits considerably heightened magnetic transitions, thus, requiring the incorporation of an exchange mean-field approach. This approach, in turn, leads to a more intricate analysis of the phonon Zeeman effect when compared to f electron systems (32). The higher magnetic transition temperature in CTO offers a unique possibility to study the connection between the nature of magnetic order and the phonon magnetic moment as revealed by the g_{ph} temperature dependence (Fig. 4*E*), unlike in rare-earth paramagnets. This difference can be partially attributed to the presence of an in-plane magnetic anisotropy in CTO. The easy-plane anisotropy leads to an exchange mean-field in the *a–b* plane that does not lift the degeneracy of chiral phonons but leads to a saturation of phonon magnetic moment at lower temperatures.

The quantum magnet CTO has drawn significant interest recently, especially in the context of topological bosonic excitations. Both magnon and SOE bands are found to be topological in inelastic neutron scattering experiments (19–21). In this work, we unravel another exotic phenomenon in this material, the giant magnetic moments for two phonon modes. We attribute this phonon chirality to the coupling of phonons to SOEs due to their

energy proximity. A large magnetic moment allows for enhanced magnetic control of phonons, e.g., selective excitation of certain phonons or manipulation of their transport properties (33). The phonon coupling to a topological SOE we explore here is an exciting topic for further investigations. Theoretical studies suggest that magnon–phonon coupling can change the phonon band topology and affect the chiral phonon transport (34). Similarly, phonons coupled to topological SOEs may also become topological and contribute to the phonon thermal Hall effect. Consistent with this idea, the recent observation of a large thermals Hall signal found in the psuedogap phase of cuprate superconductors was attributed to chiral phonons (35).

Materials and Methods

Sample Growth and Characterization. High-quality CTO single crystals were prepared using the floating zone method. A starting ceramic rod of CTO was prepared by thoroughly mixing the stoichiometric amount of CoO (99.99%, Alfa Aesar) and TiO_2 (99.99%, Alfa Aesar) and calcined at 1,000 °C in air . The crystal growth in the image furnace was carried out under a constant air flow and with 8 mm/h growth speed. The CTO single crystal was black in color with shiny surfaces. The phase purity of the as-grown CTO was verified with powder X-ray diffraction on the powder sample prepared by pulverized the crystal ingot. The crystal orientation of pellets used for Raman measurement was determined by Laue back reflection.

Spontaneous Raman Spectroscopy. Raman measurements were performed using a 532-nm excitation laser with a full-width-half maximum of 1.3 cm^{-1}. The laser power was kept below ∼0.35 mW to avoid local heating and damage to the samples. The laser beam was focused onto the sample via a 40X microscope objective to a spot size of 2 to 3 μm in diameter. The Raman signal was collected in the back-scattering geometry and measured with a Horiba LabRAM HR Evolution Raman microscope (1,800 grooves/mm grating) equipped with a thermoelectric-cooled CCD. These measurements were taken in a closed-cycle helium cryostat from 12 to 300 K with a base pressure lower than 7×10^{-7} Torr. An out-of-plane magnetic field ranging from 0 to 7 T was applied.

Data, Materials, and Software Availability. The data that support the plots within this paper and other findings of this study are available to readers in a public repository (https://osf.io/a4crv/?view_only=cfc3e27a7f8946b5a5a837cde78cf22b) (36). Source data are provided with this paper. All other data are included in the manuscript and/or supporting information.

ACKNOWLEDGMENTS. This research was primarily supported by the NSF through the Center for Dynamics and Control of Materials: an NSF Materials Research Science and Engineering Center under Cooperative Agreement No. DMR-1720595 and DMR-2308817. Additional support from NSF DMR-2114825 and the Alexander von Humboldt Foundation is gratefully acknowledged by G.A.F. This work was performed in part at the Aspen Center for Physics, which is supported by NSF grant PHY-1607611. G.Y., C.N., and R.H. acknowledge support by NSF Grant No. DMR-2104036. Part of the experiments were performed at the user facility supported by the NSF through the Center for Dynamics and Control of Material under Cooperative Agreement No. DMR-1720595 and The Major Research Instrumentation program DMR-2019130. Work in the Baldini group at UT Austin was primarily supported by the Robert A. Welch Foundation (F-2092-20220331) (to F.Y.G. for data taking) and the United States Army Research Office (W911NF-23-1-0394) (to E.B. for supervision and manuscript writing).

Author affiliations: [a]Department of Physics, Center of Complex Quantum Systems, The University of Texas at Austin, Austin, TX 78712; [b]Center for Dynamics and Control of Materials, The University of Texas at Austin, Austin, TX 78712; [c]Department of Physics, Northeastern University, Boston, MA 02115; [d]Department of Physics, Massachusetts Institute of Technology, Cambridge, MA 02139; [e]Department of Electrical and Computer Engineering, Texas Tech University, Lubbock, TX 79409; and [f]Department of Mechanical Engineering, The University of Texas at Austin, Austin, TX 78712

1. P. Thalmeier, P. Fulde, Optical phonons of rare-earth halides in a magnetic field. *Z. Phys. B, Condens. Matter* **26**, 323–328 (1977).
2. G. Schaack, Magnetic field dependent splitting of doubly degenerate phonon states in anhydrous cerium-trichloride. *Z. Phys. B, Condens. Matter* **26**, 49–58 (1977).
3. L. Du *et al*., Lattice dynamics, phonon chirality, and spin-phonon coupling in 2d itinerant ferromagnet Fe_3GeTe_2. *Adv. Funct. Mater.* **29**, 1904734 (2019).
4. B. Cheng *et al*., A large effective phonon magnetic moment in a Dirac semimetal. *Nano Lett.* **20**, 5991–5996 (2020).
5. A. Baydin *et al*., Magnetic control of soft chiral phonons in PbTe. *Phys. Rev. Lett.* **128**, 075901 (2022).
6. F. G. G. Hernandez *et al*., Observation of interplay between phonon chirality and electronic band topology. *Sci. Adv.* **9**, eadj4074 (2023).
7. Y. Ren, C. Xiao, D. Saparov, Q. Niu, Phonon magnetic moment from electronic topological magnetization. *Phys. Rev. Lett.* **127**, 186403 (2021).
8. D. Yao, S. Murakami, Chiral-phonon-induced current in helical crystals. *Phys. Rev. B* **105**, 184412 (2022).
9. T. Inoshita, H. Sakaki, Density of states and phonon-induced relaxation of electrons in semiconductor quantum dots. *Phys. Rev. B* **56**, R4355 (1997).
10. M. Du, X. Liu, S. Xie, Spin–orbit coupling and the fine optical structure of chiral helical polymers. *Phys. Chem. Chem. Phys.* **24**, 9557–9563 (2022).
11. X. Chen *et al*., Entanglement of single-photons and chiral phonons in atomically thin WSe_2. *Nat. Phys.* **15**, 221–227 (2019).
12. E. Liu *et al*., Valley-selective chiral phonon replicas of dark excitons and trions in monolayer WSe_2. *Phys. Rev. Res.* **1**, 032007 (2019).
13. H. Li *et al*., Negative magnetoresistance in Dirac semimetal Cd_3As_2. *Nat. Commun.* **7**, 10301 (2016).
14. D. M. Juraschek, N. A. Spaldin, Orbital magnetic moments of phonons. *Phys. Rev. Mater.* **3**, 064405 (2019).
15. D. M. Juraschek, T. Neuman, P. Narang, Giant effective magnetic fields from optically driven chiral phonons in 4*f* paramagnets. *Phys. Rev. Res.* **4**, 013129 (2022).
16. R. M. Geilhufe, Dynamic electron–phonon and spin–phonon interactions due to inertia. *Phys. Rev. Res.* **4**, L012004 (2022).
17. D. M. Juraschek, M. Fechner, A. V. Balatsky, N. A. Spaldin, Dynamical multiferroicity. *Phys. Rev. Mater.* **1**, 014401 (2017).
18. D. M. Juraschek, P. Narang, N. A. Spaldin, Phono-magnetic analogs to opto-magnetic effects. *Phys. Rev. Res.* **2**, 043035 (2020).
19. B. Yuan *et al*., Spin–orbit exciton in a honeycomb lattice magnet $CoTiO_3$: Revealing a link between magnetism in *d*- and *f*-electron systems. *Phys. Rev. B* **102**, 134404 (2020).
20. B. Yuan *et al*., Dirac magnons in a honeycomb lattice quantum *XY* magnet $CoTiO_3$. *Phys. Rev. X* **10**, 011062 (2020).
21. M. Elliot *et al*., Order-by-disorder from bond-dependent exchange and intensity signature of nodal quasiparticles in a honeycomb cobaltate. *Nat. Commun.* **12**, 1–7 (2021).
22. E. Kroumova *et al*., Bilbao crystallographic server: Useful databases and tools for phase-transition studies. *Phase Trans.* **76**, 155–170 (2003).
23. R. Hisatomi *et al*., Helicity-changing Brillouin light scattering by magnons in a ferromagnetic crystal. *Phys. Rev. Lett.* **123**, 207401 (2019).
24. T. Higuchi, N. Kanda, H. Tamaru, M. Kuwata-Gonokami, Selection rules for light-induced magnetization of a crystal with threefold symmetry: The case of antiferromagnetic NiO. *Phys. Rev. Lett.* **106**, 047401 (2011).
25. K. Ishito *et al*., Truly chiral phonons in *β*-HgS. *Nat. Phys.* **19**, 35–39 (2023).
26. T. Satoh, R. Iida, T. Higuchi, M. Fiebig, T. Shimura, Writing and reading of an arbitrary optical polarization state in an antiferromagnet. *Nat. Photonics* **9**, 25–29 (2015).
27. E. Oishi, Y. Fujii, A. Koreeda, Selective observation of enantiomeric chiral phonons in *β*-quartz. arXiv [Preprint] (2022). https://doi.org/10.48550/arXiv.2210.07526 (Accessed 14 October 2022).
28. S. G. Jeong *et al*., Unconventional interlayer exchange coupling via chiral phonons in synthetic magnetic oxide heterostructures. *Sci. Adv.* **8**, eabm4005 (2022).
29. E. Thingstad, A. Kamra, A. Brataas, A. Sudbø, Chiral phonon transport induced by topological magnons. *Phys. Rev. Lett.* **122**, 107201 (2019).
30. L. Zhang, Q. Niu, Chiral phonons at high-symmetry points in monolayer hexagonal lattices. *Phys. Rev. Lett.* **115**, 115502 (2015).
31. H. Zhu *et al*., Observation of chiral phonons. *Science* **359**, 579–582 (2018).
32. S. Chaudhary, D. M. Juraschek, M. Rodriguez-Vega, G. A. Fiete, Giant effective magnetic moments of chiral phonons from orbit–lattice coupling. arXiv [Preprint] (2023). https://doi.org/10.48550/arXiv.2306.11630 (Accessed 20 June 2022).
33. P. Khan, M. Kanamaru, K. Matsumoto, T. Ito, T. Satoh, Ultrafast light-driven simultaneous excitation of coherent terahertz magnons and phonons in multiferroic $BiFeO_3$. *Phys. Rev. B* **101**, 134413 (2020).
34. B. Ma, G. A. Fiete, Antiferromagnetic insulators with tunable magnon–polaron Chern numbers induced by in-plane optical phonons. *Phys. Rev. B* **105**, L100402 (2022).
35. G. Grissonnanche *et al*., Chiral phonons in the pseudogap phase of cuprates. *Nat. Phys.* **16**, 1108–1111 (2020).
36. X. Li, PNAS Spin-Orbit Exciton-Induced Phonon Chirality in a Quantum Magnet. OSF. https://osf.io/a4crv/?view_only=cfc3e27a7f8946b5a5a837cde78cf22b. Accessed 13 December 2023.